

Experimental investigation of the effect of interface angle on mode-I fracture toughness in DCB laminates using digital image correlation

Deng, Linlin; Liu, Liu; Pascoe, John Alan; Alderliesten, René

10.1016/j.engfracmech.2025.110988

Publication date

Document Version Final published version

Published in

Engineering Fracture Mechanics

Citation (APA)

Deng, L., Liu, L., Pascoe, J. A., & Alderliesten, R. (2025). Experimental investigation of the effect of interface angle on mode-I fracture toughness in DCB laminates using digital image correlation. *Engineering Fracture Mechanics*, *319*, Article 110988. https://doi.org/10.1016/j.engfracmech.2025.110988

Important note

To cite this publication, please use the final published version (if applicable). Please check the document version above.

Copyright

Other than for strictly personal use, it is not permitted to download, forward or distribute the text or part of it, without the consent of the author(s) and/or copyright holder(s), unless the work is under an open content license such as Creative Commons.

Please contact us and provide details if you believe this document breaches copyrights. We will remove access to the work immediately and investigate your claim.

FISFVIFR

Contents lists available at ScienceDirect

Engineering Fracture Mechanics

journal homepage: www.elsevier.com/locate/engfracmech



Experimental investigation of the effect of interface angle on mode-I fracture toughness in DCB laminates using digital image correlation

Linlin Deng ^{a,b}, Liu Liu ^{b,b},*, John-Alan Pascoe ^{c,b},*, René Alderliesten ^{c,b}

- ^a Beijing Key Laboratory of Civil Aircraft Structures and Composite Materials, COMAC Beijing Aircraft Technology Research Institute, Beijing, PR China
- ^b School of Aerospace Engineering, Beijing Institute of Technology, Beijing, PR China
- ^c Aerospace Structures & Materials Department, Faculty of Aerospace Engineering, Delft University of Technology, Kluyverweg 1, 2629 HS Delft, The Netherlands

ARTICLE INFO

Keywords: Mode-I fracture toughness Interface angle Correlation function Traction-separation law Zigzag crack

ABSTRACT

This study investigates the Mode-I fracture toughness of laminates with varying interface angles. A method for identifying crack tip location using grayscale characteristic parameters in DIC is proposed. The findings demonstrate that both initial and steady-state fracture toughness exhibit a bilinear relationship with interface angle. A cohesive constitutive model incorporating the interface angle was developed and integrated into a double cantilever beam finite element model, predicting delamination propagation behavior that was highly consistent with experimental results. Numerical analysis suggests that zigzag cracks may improve fracture toughness before steady-state toughness is achieved, with peak toughness correlating to the length of the zigzag cracks.

1. Introduction

Fiber-reinforced epoxy matrix composite materials are widely used in aircraft structures and small unmanned aerial vehicles due to their high specific strength and stiffness, fatigue resistance, and design flexibility. The application has progressed from secondary to primary load-bearing structures like wings and fuselages [1–5]. Because of a lack of reinforcement in the thickness direction, composite laminates' interlaminar mechanical properties are significantly lower than their in-plane properties, resulting in delamination cracks as a common failure mode. Residual stress during laminate manufacturing, elevated temperatures and humidity, low-speed impacts, out-of-plane loads, and design material and structural discontinuities, such as free edges, openings, and abrupt changes in laminate thickness, can all cause delamination cracks. Delamination cracks significantly weaken the laminate, compromising the overall integrity and safety of the aircraft structure. It restricts the use of composites in load-bearing aircraft structures [6–8].

Recent studies have extensively examined the delamination mechanism of composite laminates subjected to mode-I loading through double cantilever beam (DCB) testing [9–15]. For instance, Ardakani-Movaghati et al. [16] and Sabaghi et al. [17] demonstrated that incorporating nano-silica particles into the matrix material and increasing the operating temperature significantly enhanced the Mode I fracture toughness of glass/epoxy composite laminates. Hosseini et al. [18] studied delamination crack propagation at the interface of woven glass/epoxy composites with an interlayer under Mode I loading, finding that the interlayer significantly altered the crack propagation mechanism, reducing fracture toughness by 80% at initiation and 69% at propagation. Hu et al. [19] proposed an edge effect mitigator for investigating Mode I fracture toughness in multidirectional laminates. This

E-mail addresses: liuliu@bit.edu.cn (L. Liu), J.A.Pascoe@tudelft.nl (J.-A. Pascoe).

https://doi.org/10.1016/j.engfracmech.2025.110988

^{*} Corresponding authors.

Nomenclature	
DCB	Double cantilever beam
DIC	Digital image correlation
VCCT	Virtual crack closure technique
MBT	Modified beam theory
CC	Compliance calibration method
MCC	Modified compliance calibration
COD	Crack opening displacement
θ	Interface angle
E_1, E_2, E_3	Elastic modulus
G_{12}, G_{13}, G_{23}	Shear modulus
v_{12}, v_{13}, v_{23} v_{12}, v_{13}, v_{23}	Poisson's ratio
C_{sub}	Grayscale correlation parameter of the DIC technique
$f(x_i, y_i)$	Grayscale value of the pixel <i>i</i> in the reference subset
$g(x_i', y_i')$	Grayscale value of the pixel <i>i</i> in the deformed subset
$g(x_i, y_i)$ m	Total number of pixels within the subset in the DIC technique
$ar{f}$	Average grayscale value of the reference subset
$ar{g}$	Average grayscale value of the deformed subset
e P	Applied load in DCB test
B	Specimen width
h	Specimen thickness
C	Ratio of the load point displacement to the applied load
A_1	A least squares plot of \bar{a}/h as a function of the cube root of compliance
\bar{a}	Distance between the DCB specimens loading point and the crack tip
a	Crack growth length
	Initial crack length
$a_0 \ LLG_I^0$	Initial fracture toughness
	Mode-I fracture toughness in the DCB test
G_I G_I^{ss} G_I^b δ^*	Steady state fracture toughness
G^b	Fracture toughness caused by the fiber bridging
$\delta_I^{}$	COD at the initial crack tip
δ	COD at the crack propagation path
δ_0	COD at the initial interface damage
δ_1	COD at the onset of damage of the bridging fiber
δ_f	COD at the interface final failure
σ^c	Interface cohesive stress
σ^c_{max}	Maximum cohesive opening traction stress
σ_{max}^{b}	Maximum fiber bridging stress
max k	The initial interfacial stiffness
$G_a, G_b, \delta_a, \delta_b$	Fitting parameters of the exponential cohesive constitutive model for the fiber-bridging zone
a_{Z}	Zigzag crack length
a_I	Intralaminar crack length
α	Zigzag crack with an inclination angle
$ar{\delta}$	Zigzag crack length along the interface

mitigator functions by restricting both intralaminar and interlaminar damage coupling, limiting delamination crack propagation to the design interface. This approach enables a more objective and accurate assessment of delamination crack behavior. Gracia et al. [20] analyzed the interlaminar fracture of angle-ply symmetric and anti-symmetric laminates using the double cantilever beam test. An expression for determining the energy release rate in both cases has been obtained based on their analysis.

The method of determining the grayscale correlation of an image can reduce the influence of errors caused by manual crack length measurement [21–24]. Gorman and Thouless [25] proposed analyzing an adhesively bonded DCB using the DIC method and determining the traction–separation law for a cohesive-zone model (CZM). Blaysat et al. [26] proposed a procedure to identify spatial interfacial traction profiles of peel-loaded DCB specimens and extract the corresponding traction–separation relation. The robustness of their procedure in the presence of noisy data, as well as its low sensitivity to the initial guess, is demonstrated by post-processing virtually deformed images generated using a finite element method. Huo et al. [27] developed a DIC-VCCT method capable of accurately determining the fracture energy release rate for crack-metal joints and composite laminate structures using displacement data obtained from DIC measurements. This method eliminates the need for additional input such as geometry, load, or boundary conditions. They demonstrate that using a CZM with the measured traction–separation law and an appropriate compressive regime provides accurate predictions for the deformation ahead of the crack tip.

Table 1
The elastic properties of cured M30SC-150/DT120-34F carbon/epoxy prepreg [38.39].

				<u> </u>					
Laminated composite	E_1 (GPa)	E_2 (GPa)	E_3 (GPa)	G ₁₂ (GPa)	G ₁₃ (GPa)	G ₂₃ (GPa)	ν_{12}	ν_{13}	ν_{23}
M30SC-150/DT120-34F	155.0	7.8	7.8	5.50	5.50	3.92	0.29	0.29	0.487

Finite element numerical simulation can include the delamination of fiber-reinforced composite laminates in the model, allowing for a low-cost analysis of the delamination crack propagation behavior of complex structures. Common numerical fracture analysis techniques include the cohesive zone method (CZM) [28–30], the VCCT [31,32], and the Extended Finite Element Method (XFEM) [33,34]. Airoldi and Dávila [35] studied two methods for calculating the shape parameters of cohesive laws. They proposed that by superposing two cohesive elements with different linear softening laws, they could represent the resistance curves that characterize damage phenomena as they progress from delamination crack initiation to steady-state propagation. Yolum et al. [36] used peridynamic (PD) theory to model mode-I delamination cracks in unidirectional and multidirectional laminated composites. Under mode-I loading conditions, force–displacement relations and delamination crack migration in multidirectional laminated composites were successfully described using PD theory with a bilinear softening law. Sohrabi et al. [37] developed a new approach to predict the load–displacement curve of the $0^{\rm o}//90^{\rm o}$ interface in the cross-ply laminated composite in the FEA software ABAQUS. The load–displacement curve of the $[0_5/90/0_6]$ stacking sequence can be predicted by incorporating hardening mechanisms such as zigzag crack growth, fiber bridging, and fiber-resin adhesion in the finite element analysis.

Researchers have conducted some experimental and numerical studies on how the delamination interface angle influences the propagation of delamination cracks in laminates. However, we still do not fully understand how the interface angle affects the fracture toughness of multidirectional laminates. Most studies focus on the impact of common interface fiber angles on fracture toughness, such as the change in fracture toughness with delamination crack length and fiber bridging behavior at interface angles of $0^{\circ}//45^{\circ}$ or $0^{\circ}//90^{\circ}$. Not much research has been done on fracture toughness at the general interface angle, and the dataset for mode-I fracture toughness does not cover the whole range from $0^{\circ}//0^{\circ}$ to $0^{\circ}//90^{\circ}$. So far, there is not a clear link between mode-I fracture toughness and interface angle. Also, we do not know how the fiber bridging mechanism affects the cohesive constitutive parameters at different interface angles.

To address the issues and determine the mode-I fracture toughness at different interface angles, DCB tests on carbon fiber epoxy matrix laminates with various interface angles were first performed. A new method for measuring delamination crack length is proposed, based on the grayscale correlation function of subsets in the DIC method. The results were confirmed using the virtual extensometer. It has been discovered that when interface delamination with different fiber angles propagates unstably due to fiber bridging, the mode-I fracture toughness changes in various patterns. The evolution of mode I fracture toughness in laminates with interface angles ranging from $0^{\circ}//0^{\circ}$ to $0^{\circ}//90^{\circ}$ is developed, and an interface angle-related constitutive model for cohesive zones is established. For multidirectional laminates, an explicit relationship between mode-I fracture toughness and interface fiber angle is derived using the cohesive traction–separation law of the interface. As a result, a model for predicting mode-I fracture toughness for different interface fiber angles is developed and validated. A finite element model with a zigzag crack at the $0^{\circ}//90^{\circ}$ interface was developed. When combined with the constitutive relationship of the interface proposed in the work, a correlation between the toughening mechanism of mode-I fracture toughness for laminate composites and zigzag crack propagation is demonstrated.

2. Experiments

2.1. Double cantilever beam specimen

The specimen for this study was made by hand-laying up from a prepreg of carbon fiber M30SC-150 and epoxy matrix DT120-34F (supplied by Delta-Tech S.p.A Italy). Table 1 presents the elastic parameters [38,39]. Laminated panels were prepared by stacking 32 plies of prepreg using the stacking sequence of $[0_{15}//\theta//0_{16}]$ ($\theta=0^{\circ}$, 15° , 30° , 45° , 60° , and 90°). According to reports by Shokrieh et al. [40], Pereira et al. [41], and Andersons et al. [42], when the interface angle exceeds 60° , the fracture toughness in the initial and stable stages of crack propagation rarely changes. As a result, when the interface angle exceeded 60° , we skipped the $0^{\circ}//75^{\circ}$ experiment and proceeded directly to the $0^{\circ}//90^{\circ}$ experiment. During stacking, a Teflon insert of 12.7 μ m thickness and 60 mm length was placed at the edge of the panel between the 15th and 16th ply to act as an initial crack. The panel was cured in an autoclave at a pressure of 6 bars and a curing temperature of 120° for 90 min. The material supplier recommended the cure cycle for the laminate. The cured ply thickness was approximately 0.156 mm, yielding a 5.0 mm panel thickness after curing.

Following curing, the panel was ultrasonically scanned for flaws. DCB specimens were cut from the panel's defect-free areas using a water jet cutting. The research refers to ASTM D5528 [9] for the design of DCB test specimens. The dimensions of the specimen in this study were selected as $200 \text{ mm} \times 25 \text{ mm} \times 5 \text{ mm}$, with an initial crack length a_0 of 60 mm, as illustrated in Fig. 1(b). The exact location of each pre-existing crack on each specimen was determined step by step using an optical microscope and marked with a vertical line. To facilitate hinge fastening, aluminum tabs were bonded to the specimens. After preparing the specimen, the cutting surface was polished with fine sandpaper. The area for attaching the aluminum load blocks was sanded with coarse sandpaper and then cleaned with acetone.

To ensure the accuracy of the measured fracture toughness, the delamination crack propagation lengths on both sides of the specimen were measured concurrently, and the fracture toughness was calculated separately for each side. As a result, the fracture

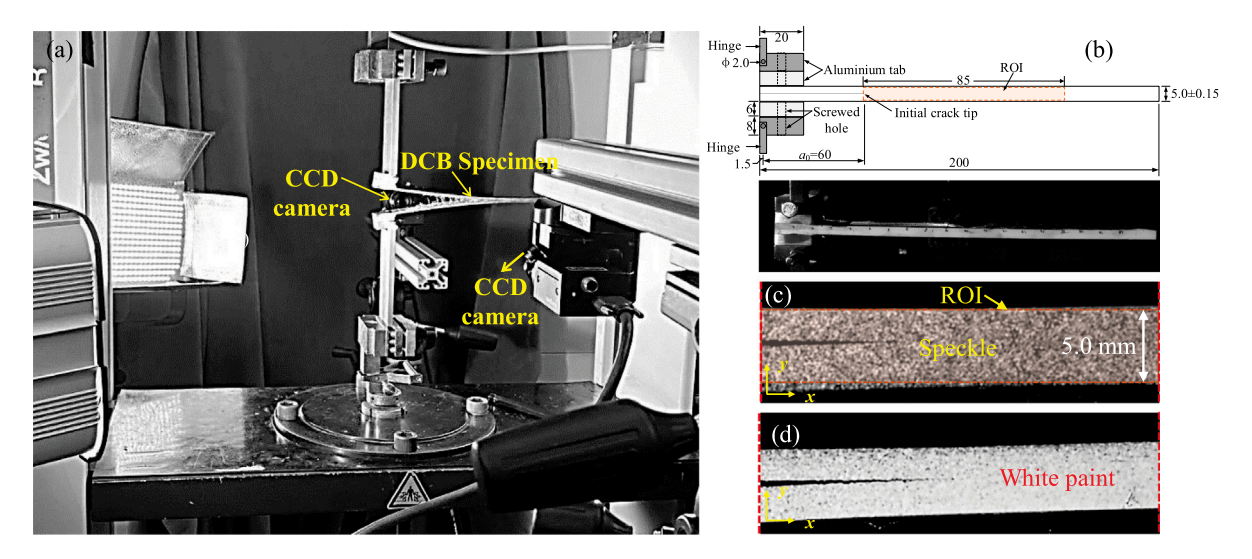


Fig. 1. Experimental setup of a double cantilever beam (DCB). (a) The fixture of the DCB test; (b) The dimension of the DCB test specimen; (c) A zoomed-in view of the DCB specimen's speckle pattern; (d) A zoomed-in view of the white paint.

toughness of the specimen can be calculated by averaging the two side fracture toughnesses [43]. Speckles were sprayed on one side of the specimen to measure deformation during delamination crack propagation, as shown in Fig. 1(c). To enhance crack tip visibility, a thin white correction fluid was painted on the other side of each specimen (xreffig1(d). The thin white layer is more brittle than the composites, so it always fractures with the real crack. A strip of millimeter-sized paper with a grid size of 1 mm \times 1 mm was pasted on both sides of the specimen to measure the length of the delamination crack. The millimeter paper was estimated to have a 1% error per millimeter. Fig. 1(b) depicts images of DCB specimens. Following the experiment, the delamination crack length on the white paint side was measured with visual inspection and ImageJ software. The delamination crack length on the speckle side was determined using the DIC method. Section 2.3 explains how to measure delamination crack length using DIC.

2.2. DCB test setup and procedure

The quasi-static DCB test was carried out using a 20 kN hydraulic Zwick static test machine in accordance with ASTM 5528 [9]. A monotonic displacement-control load is applied to the specimen at a rate of 1 mm/min. The specimens were secured in the machine clamps with a pair of splittable hinges. The hinge has a removable pin that serves as a joint between its plates. One hinge plate was bolted to the specimen and the other clamped into the machine. The Digital Image Correlation (DIC) technique was used to measure deformation in the DCB experiment. Fig. 1(a) shows the test setup with two 2D-DIC systems on both sides of the specimen. The 2D-DIC system depicted in Fig. 1(a) includes a 4 MP CCD camera and a Tamron 50 mm lens. The camera sensor has a 2048 × 2048 array of pixels and a physical sensor size of 5.9 μ m × 5.9 μ m. The imaging system was mounted on a translation stage and set to focus on a region close to the crack tip. The object distance was approximately 500 mm. The camera was positioned so that its plane was parallel to the specimen's observation surface and covered the entire length of its field of view. The Q400-DIC system (LIMESS Messtechnik und Software GmbH) was used to capture two images per second while the specimen was subjected to a monotonic load. As a result, 200–300 images were acquired for delamination crack length measurement. The tests for specimens with different interface angles were conducted four times, resulting in 24 DCB experiments.

2.3. The measurement of delamination crack length using the DIC

The DIC technique is widely used in mode I fracture toughness tests of composite materials, and the DIC-based virtual extensometer method for determining crack propagation length is well accepted [24,25,44–46]. It calculates the crack opening displacement (COD) by determining the relative displacement between the crack's two sides, which is then used to locate the crack tip and calculate the crack propagation length. As the crack tip is approached, the relative displacement, δ , gradually decreases until it reaches zero. The crack tip is the point where the COD reaches zero, as indicated in Fig. 2. As a result, when using the virtual extensometer method to determine the crack propagation length, multiple extensometers must be used along the crack propagation path and ensure that the crack tip area is included.

Thus, the virtual extensometer method was first used in the study to determine the COD of delamination cracks. On the DCB specimen, a series of virtual extensometers A_i (i = 1, 2, ..., n) were set up with a spacing of 1.45 mm (20 pixels) along the x direction of the delamination extension path, and their spatial distribution is shown in Fig. 2(a). As a result, a total of 58 sets of virtual extensometers were used to track the 85-mm crack growth path of the DCB specimen, as shown in Fig. 1(b). Two measuring areas (2 mm \times 2 mm) were placed 1 mm above and below point A_i along the path of the delamination crack, as shown in the

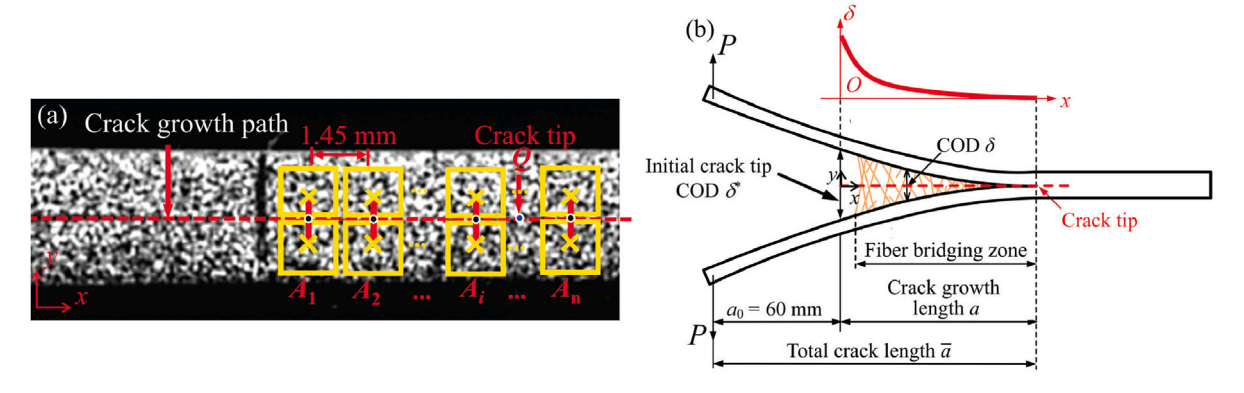


Fig. 2. (a) A schematic diagram of the virtual extensometer method for determining crack opening displacement; (b) A schematic diagram of the fiber bridging zone behind the crack tip.

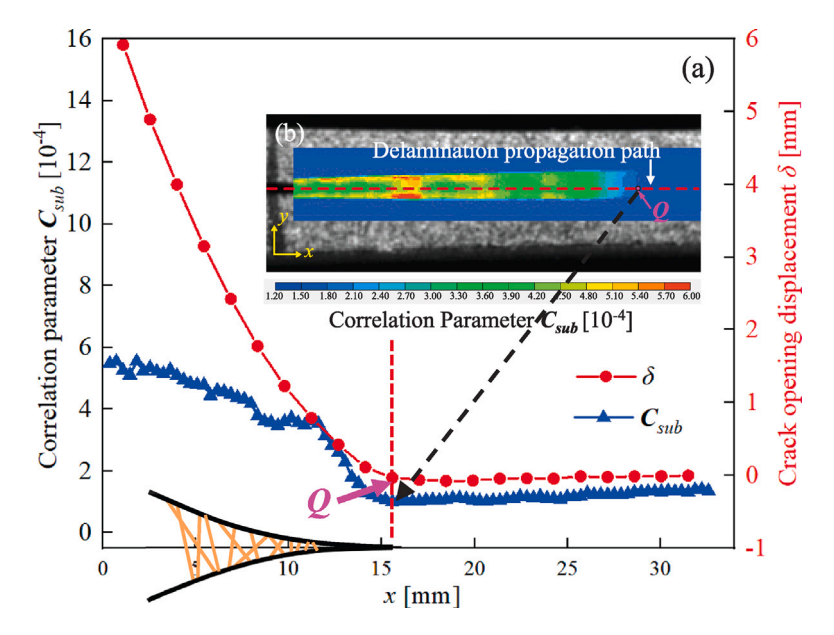


Fig. 3. (a) Variations in relative open displacement δ and correlation parameter C_{sub} along the delamination growth path passing over the tip in the fiber bridging zone. The x-axis definition corresponds to the x-axis in red in Fig. 2(b). The coordinate's origin is the position of the initial crack tip, and x represents the distance from it; (b) The typical distribution of the subset correlation parameter distribution.

yellow boxes in Fig. 2. The relative displacement in the y-direction at the midpoint of the two regions was calculated to represent the COD at point A_i along the delamination crack path.

During data processing using the virtual extensometer method, the relative displacement of all virtual extensometers in the deformation image must be calculated throughout the loading process. After acquiring relative displacement from 58 sets of virtual extensometers, the variation of COD with respect to the x-coordinate at a specific loading time can be given. Determining the position at which COD approaches zero enables the identification of the crack tip's location at the specific time. The COD curve for the $0^{\circ}//45^{\circ}$ specimen along the crack propagation path is shown in Fig. 3(a), which was measured under a load of 90.254 N with a displacement of 8.3 mm using the virtual displacement extensometer method. The crack tip is 15.57 mm away from the initial crack tip, indicating that the crack opening displacement curve approaches zero (point Q in Fig. 3(a)). To determine the crack propagation length using the virtual displacement extensometer, multiple sets of virtual extensometers must be placed along the crack propagation path, with the range including the crack tip. As a result, each deformation image must calculate the gauge point's relative displacement multiple times (equal to the number of virtual extensometers), making the operation time-consuming.

To address the high data processing demands of the virtual extensometer method, a rapid crack tip identification method based on the grayscale correlation parameter of the subset in the DIC is proposed in the study. It can directly and quickly determine the crack tip position and calculate the crack length without the need for multiple virtual extensometers along the crack path, which increases efficiency. First of all, the DIC technique captures deformation by tracking the motion of the same region (subset) in images taken before and after deformation. Accurate deformation measurement relies on the correct matching of the corresponding subset

in the reference image to the deformed image. Grayscale characteristic matching is a commonly used matching technique. It employs correlation parameters as a metric to identify the regions with the highest correlation in before and after deformation images. The zero-mean normalized sum of squares functions are used as correlation parameters to match the grayscale characteristics of subsets before and after deformation. The closer the correlation parameter value is to zero, the higher the correlation between the two subsets. The following expression is used to calculate the correlation parameter [47]:

$$C_{sub}[f(x,y),g(x',y')] = \sum_{i=-m}^{m} \sum_{j=-m}^{m} \left[\frac{f(x_i,y_i) - \bar{f}}{\sqrt{\sum_{i=-m}^{m} \sum_{j=-m}^{m} [f(x_i,y_i) - \bar{f}]^2}} - \frac{g(x_i',y_i') - \bar{g}}{\sqrt{\sum_{i=-m}^{m} \sum_{j=-m}^{m} [g(x_i',y_i') - \bar{g}]^2}} \right]^2$$
(1)

where $f(x_i, y_i)$ represents the grayscale value of the pixel i in the reference subset, and $g(x_i', y_i')$ denotes the grayscale value of the pixel i in the deformed subset, where \bar{f} represents the average grayscale value of the reference subset, and \bar{g} denotes the average grayscale value of the deformed subset, where m denotes the total number of pixels within the subset. The crack opening (delamination) causes discontinuous deformation, making it difficult to correlate the subsets at the interface along the delamination crack propagation path. Thus, the correlation parameter is significantly higher than zero. As it gets closer to the crack tip, the effect of discontinuous deformation on the correlation parameter fades until it disappears fully. The correlation parameter gradually decreases until it reaches its minimum value at the crack tip.

Secondly, the initial crack tip is chosen as the starting point and selected an ROI area of 85 mm in length and 5 mm in width along the crack propagation direction, as shown in Fig. 1(b). The subset size is set to 21×21 pixels² with a speckle image resolution of 0.0724 mm/pixel. This corresponds to a subset size of 1.5 mm². The step size is two pixels (0.145 mm). Each image in the ROI has about 18,000 data points. Finally, the subset grayscale correlation parameter method can be used to determine the crack tip position, eliminating the need to calculate the relative displacement of multiple virtual extensometer sets for each deformation image.

The blue triangle data points in Fig. 3(a) illustrate the distribution of the grayscale correlation parameter Csub along the crack propagation path (indicated by the red dashed line in Fig. 3(b)) for the $0^{\circ}//45^{\circ}$ specimen subjected to a load of 90.254 N and a displacement of 8.3 mm. The left ordinate represents the subset's grayscale correlation parameters with an order of magnitude of 10^{-4} . The right ordinate represents the COD determined using the virtual extensometer method. The comparison shows that the subset grayscale correlation parameter (C_{sub}) follows the same variation pattern as the COD along the crack propagation path. Point Q is the inflection point of the subset grayscale correlation parameter curve, where the COD curve approaches to its minimum. The crack is completely closed at the inflection point, and the deformation is continuous, causing the COD and subset grayscale correlation parameter to approach a minimum. Therefore, we can determine the delamination crack tip using the inflection point of the subset grayscale correlation parameter's curve. Compared to the virtual extensometer method, this method significantly reduces data processing and increases measurement efficiency while preserving the accuracy of crack propagation length measurements.

2.4. Determination of the opening mode-I fracture toughness

The ASTM D5528 test standard [9] recommends three methods for calculating the opening mode-I interlaminar fracture toughness G_I of composite materials during the DCB test. These include the modified beam theory (MBT), the compliance calibration technique (CC), and the modified compliance calibration (MCC). In this study, it is reported that G_I determined by the three data reduction methods differed by no more than 3.1%. Thus, the mode-I interlaminar fracture toughness was determined using the MCC approach. The mode-I fracture toughness G_I can be calculated as follows [9]:

$$G_I = \frac{3P^2C^{\frac{2}{3}}}{2A_1Bh} \tag{2}$$

P denotes the applied load. The compliance C represents the ratio of load point displacement to applied load. B is the specimen width, h is the specimen thickness, and A_1 is the least squares plot of \bar{a}/h as a function of the cube root of compliance, $C^{\frac{1}{3}}$. The distance between the loading point of the DCB specimen and the crack tip is \bar{a} , which can be calculated by adding the crack propagation length a and the starting crack length a_0 .

2.5. The mode-I fracture toughness determined using DCB specimens with different interface angles

Fig. 4 shows how the mode-I interlaminar fracture toughness G_I varies with the delamination crack growth length a and the crack opening displacement at the initial crack tip δ^* for DCB specimens with different interface angles. a and δ^* were measured using the DIC method. After the crack tip has been identified based on the location where the correlation parameter C_{sub} drops to a minimum, a is measured as the distance between the initial crack tip and the current crack tip. The initial crack opening displacement, δ^* , was measured through the virtual extensometer. It is noted that as the delamination crack grows from the insert, the calculated G_I increases and then stabilizes with further delamination crack growth. It indicates a fracture occurs with increased resistance. The primary reason for the increasing resistance is the development of fiber bridging, as shown in Fig. 5. These bridging fibers shield the crack tip and carry a portion of the load at the crack tip. As a results, the interlaminar fracture toughness increases for various interface angles. As the interfacial delamination crack increases further, newly generated bridging fibers in the delamination area and failed bridging fibers reach a stable equilibrium state, resulting in stable fiber bridging. So the interlaminar fracture toughness

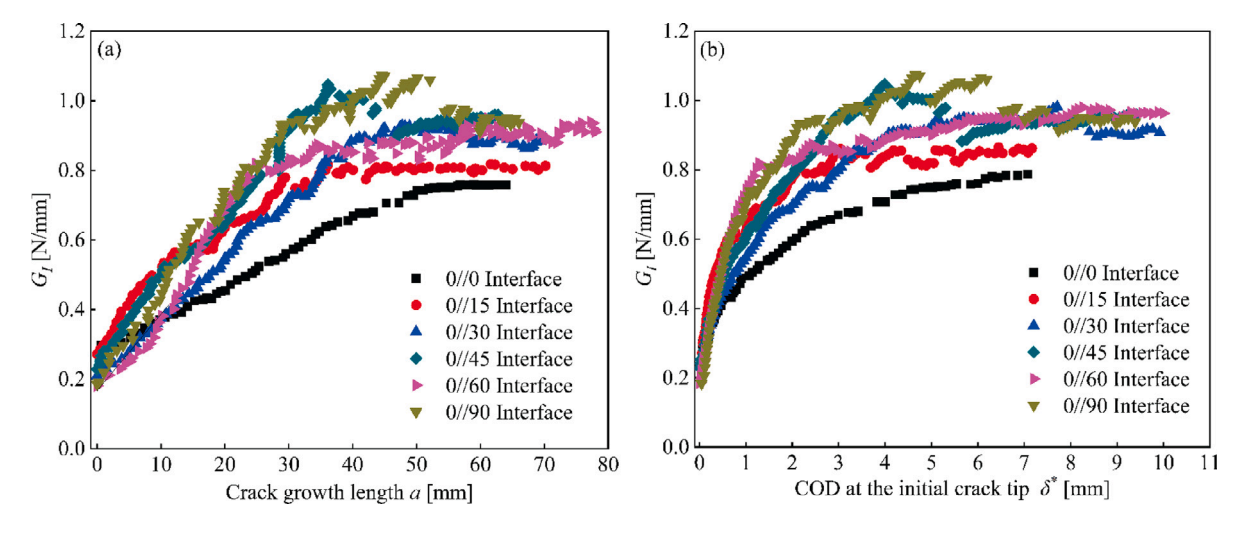


Fig. 4. The variation of the opening mode-I fracture toughness G_I with (a) the delamination crack growth length a and (b) the initial crack opening displacement \mathcal{E}^*

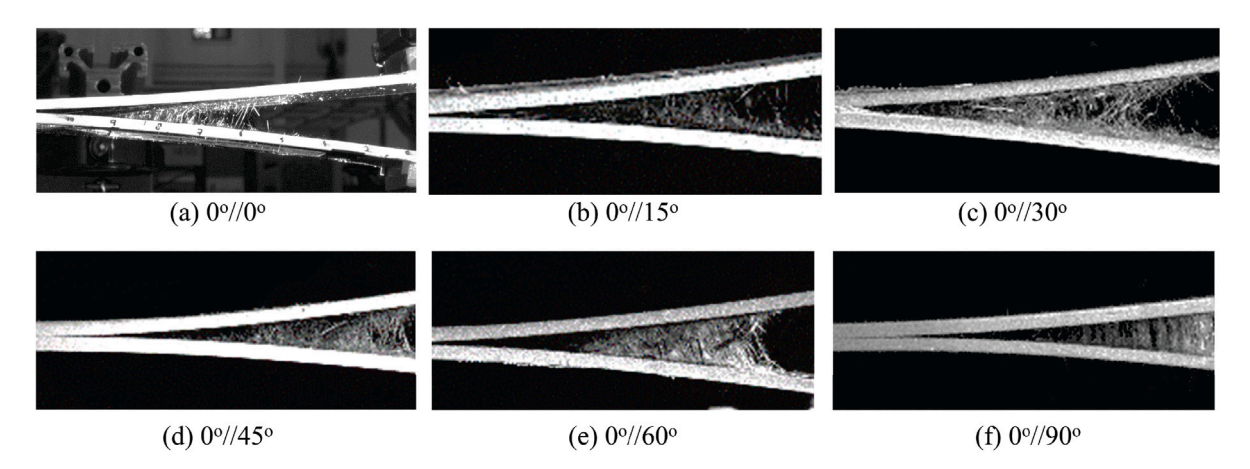


Fig. 5. Typical DCB test photographs of specimens with different interface angles, which demonstrates significant fiber bridging mechanism.

Table 2 The statistical values of fracture toughness $G_{\rm IC}$.

Interface angle θ	$G_{\rm IC}^0$ [N/mm]	$G_{\rm IC}^{ss}$ [N/mm]
0°//0°	0.286 ± 0.001	0.792 ± 0.001
0°//15°	0.272 ± 0.001	0.861 ± 0.020
0°//30°	0.230 ± 0.001	0.933 ± 0.013
0°//45°	0.228 ± 0.002	0.928 ± 0.031
0°//60°	0.185 ± 0.018	0.933 ± 0.023
0°//90°	0.183 ± 0.002	0.936 ± 0.011

reaches a steady state. A plateau in the final stage of the fracture toughness variation curve represents the steady-state fracture toughness G_I^{ss} . It is noted that when the interface angle exceeds 30°, there is little difference in steady-state fracture toughness between different interface angles. The steady-state fracture toughness of 0° and 15° interface angles is lower than that of other interface angles. G_I^{ss} of 0° interface angle is the lowest. It can also be seen that the fracture toughness G_I increases when the delamination crack growth length is between 40 and 55 mm. It then drops to a lower steady-state value when the interface angles are 45° and 90°. Section 4.3 will provide a detailed discussion of the mechanism that led to this transition.

Table 2 lists the statistical values for the initial fracture toughness G_I^0 and the steady state fracture toughness G_I^{ss} for specimens with varying interface angles. The results indicate that when the interface angle is less than 60°, the initial fracture toughness decreases approximately linearly with an increase in the interface fiber angle, whereas when the interface angle is between 60° and 90°, the initial fracture toughness remains nearly constant as the interface fiber angle increases. When the interface fiber angle

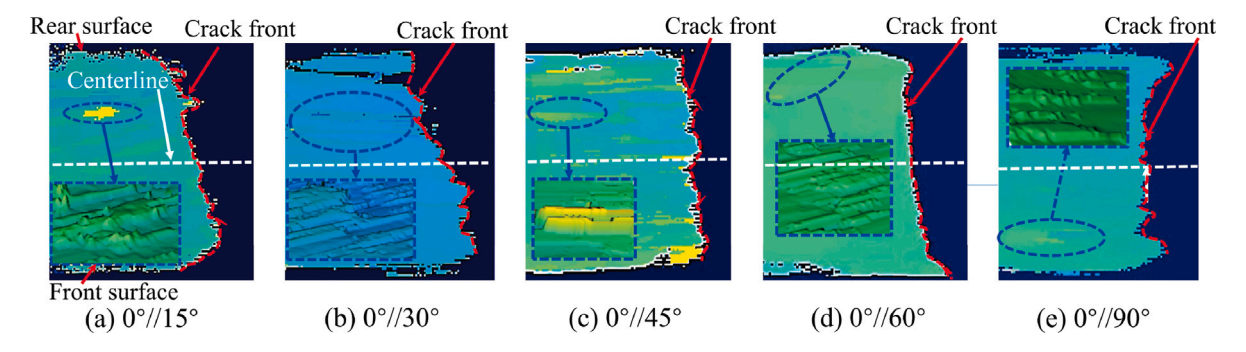


Fig. 6. C-scan of the DCB specimen's ply fracture front.

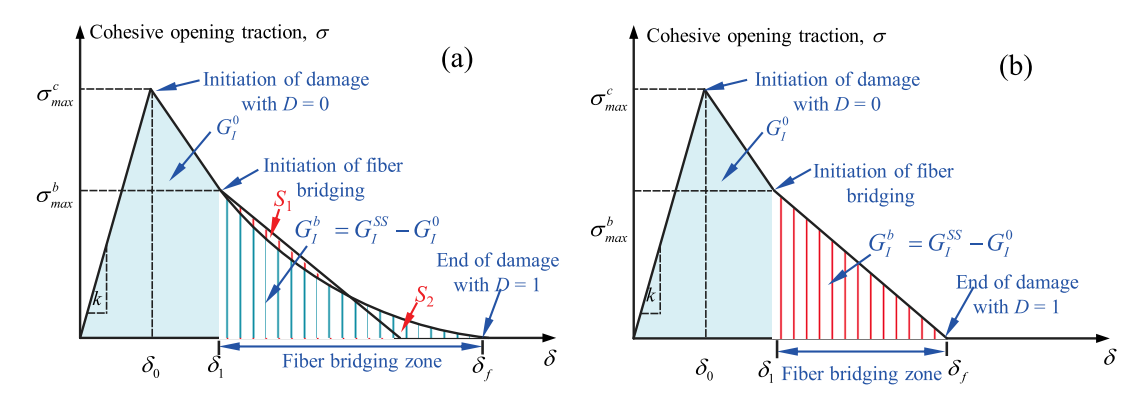


Fig. 7. (a) Schematic diagram of the nonlinear cohesive traction separation model; (b) Schematic diagram of the tri-linear cohesive traction separation model.

is less than 30° , the fracture toughness G_I^{ss} in the stable growth stage increases as the angle increases. When the interface angle exceeds 30° , the steady-state fracture toughness varies little during the stable growth stage.

Fig. 6 shows the morphology of the DCB specimen's ply fracture front as examined with an ultrasonic C-scan. Completely bonded areas are shown in dark blue, the white dashed line represents the centerline along the specimen's width, and the red dashed line indicates the crack front, with the delamination crack propagation direction from left to right. The crack fronts of the 0°//15°, 0°//30°, 0°//45°, and 0°//60° specimens are approximately inclined, whereas the crack front of the 0°//90° specimen is nearly perpendicular to the specimen's centerline. The fracture front exhibits fluctuations along the width direction for specimens with different interface angles. For example, for a specimen with an interface angle of 15°, the fracture front near the front surface lags behind other positions along the width of the specimen. For specimens with interface angles of 60° and 90°, the fracture fronts at the front and rear surfaces are higher than near the center along the width of the specimen. Non-uniform echo pulse phenomena are observed at specific locations in the C-scan patterns for specimens with different interface angles, indicating that zigzag propagation occurs during the delamination crack formation process.

3. Cohesive constitutive model of the fracture toughness with different interface angles

This work suggests a simple interface angle-dependent tri-linear cohesive constitutive model that can characterize how delamination cracks propagate at different interface angles. First, the bi-linear relationship between the initial and steady-state fracture toughness with the interface angle is developed through interpolation of results obtained from DCB tests with different interface angles, and then the simplified tri-linear cohesive constitutive model can be built to characterize the relationship between the cohesive opening traction σ and the crack opening displacement δ for specimens with interface angles ranging from 0° to 90°. The proposed model has been verified by one additional test result, which has not been used to develop the cohesive constitutive model.

3.1. The cohesive constitutive model

The phenomenological constitutive model for the fiber-bridging zone of the interface can be characterized by the cohesive traction–separation model [48]. The model describes the relationship between the cohesive traction and the crack opening displacement. Fig. 7(a) shows a schematic diagram of the exponential constitutive model for the fiber-bridging zone. It is noted that the cohesive opening traction σ increases linearly with the crack opening displacement δ until it reaches the maximum cohesive opening traction σ_{max}^c without causing any damage, where the damage variable is zero with D=0. Then, the interface damage

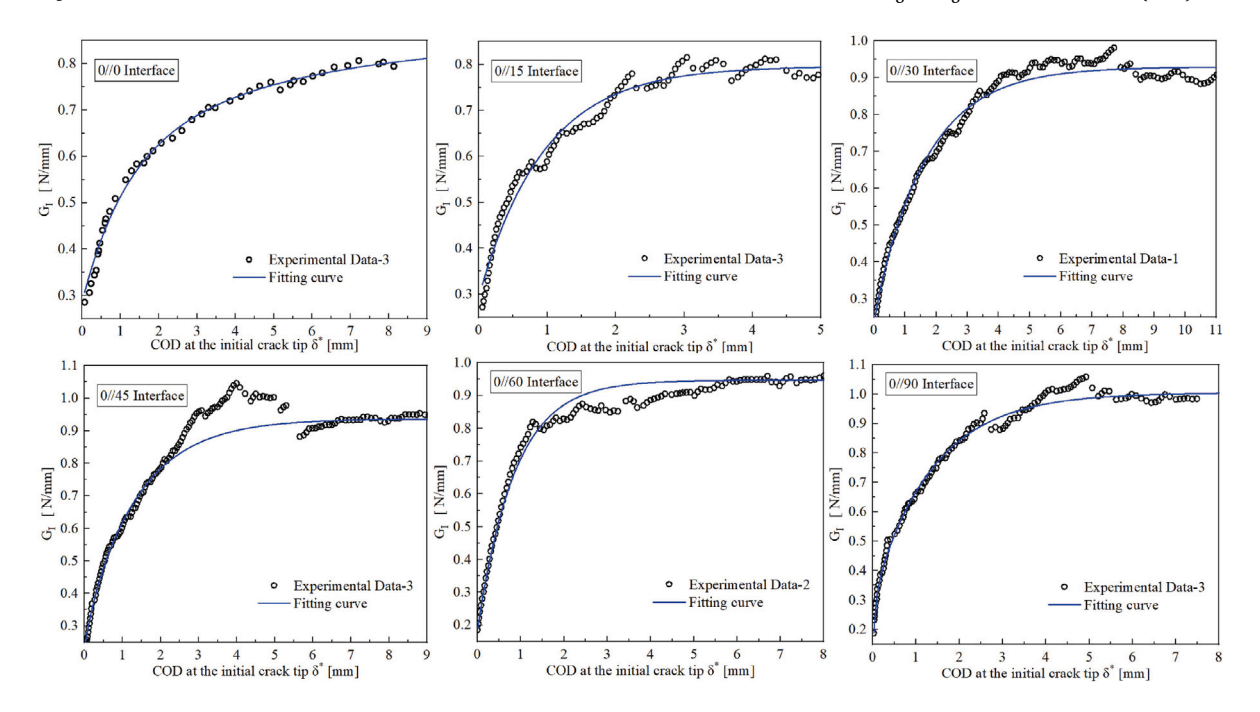


Fig. 8. Comparisons of the fracture toughness variation with crack opening displacement at the initial crack tip obtained the DCB experiment and the fitting curve for typical DCB specimens. (a) $0^{\circ}//0^{\circ}$; (b) $0^{\circ}//15^{\circ}$; (c) $0^{\circ}//30^{\circ}$; (d) $0^{\circ}//45^{\circ}$; (e) $0^{\circ}//60^{\circ}$; (f) $0^{\circ}//90^{\circ}$.

Table 3 Fitting parameters in Eq. (3) and the bridging stress σ_{mer}^{b} for DCB specimens with different interface fiber angles.

01	1 ()	max			0
Interface angle, θ	G_a [N/mm]	G_b [N/mm]	δ_a [mm]	δ_b [mm]	σ_{max}^{b} [MPa]
0°//0°	0.3147	0.2663	4.0902	0.8651	0.3073
0°//15°	0.0223	0.5021	0.0016	0.9490	0.5003
0°//30°	0.6761	0.0230	1.6735	0.1082	0.5585
0°//45°	0.6556	0.0535	1.3796	0.8651	0.7502
0°//60°	0.1207	0.6408	0.8699	0.8621	0.8810
0°//90°	0.7435	0.0704	1.1543	0.1220	1.0200

initiates and continues to increase, which causes the cohesive opening traction to decrease linearly with increasing crack opening displacement. When the cohesive opening traction reaches the maximum bridging stress σ_{max}^b corresponding to the crack opening displacement δ_1 , the fiber bridges initiate. The light blue area covered by the diagram of the cohesive opening traction and the crack opening displacement before the fiber bridges begin represents the initial fracture toughness (G_I^0). Fiber bridging reduces the growth of interface damage since they carry a portion of the load that does not reach the crack tip. The cohesive opening traction decreases nonlinearly with increasing crack opening displacement. The fiber bridging model develops from the occurrence of fiber bridging until the end of the cohesive zone with the crack opening displacement δ_f , where the cohesive opening traction decreases to zero and the interface is completely damaged with D=1. The shaded, light-red area under this region corresponds to the dissipation energy in the fiber-bridging zone. An exponential decay function, which characterizes how the fracture toughness G_I varies with the initial crack opening displacement δ^* in the fiber bridging region, is shown as follows [48,49]:

$$G_I(\delta^*) = G_a \left(1 - e^{-\frac{\delta^*}{\delta_a}} \right) + G_b \left(1 - e^{-\frac{\delta^*}{\delta_b}} \right) + G_I^0 \tag{3}$$

where G_a , G_b , δ_a , and δ_b are four fitting parameters with no physical significance and unrelated to the interface angle. The parameters for different interface angles can be obtained by fitting the measured data between the fracture toughness G_I and the initial crack opening displacement δ^* in Fig. 4(b) using the least squares approach, which is listed in Table 3. Fig. 8 compares fracture toughness variation with crack opening displacement at the initial crack tip using the DCB experiment and fitting curve.

Based on the relationship between fracture toughness and initial crack opening displacement, the bridging stress in the fiber bridging region can be calculated with:

$$\sigma_b(\delta^*) = \frac{dG_I(\delta^*)}{d\delta^*} = \left(\frac{G_a}{\delta_a}\right) e^{-\frac{\delta^*}{\delta_a}} + \left(\frac{G_b}{\delta_b}\right) e^{-\frac{\delta^*}{\delta_b}} \tag{4}$$

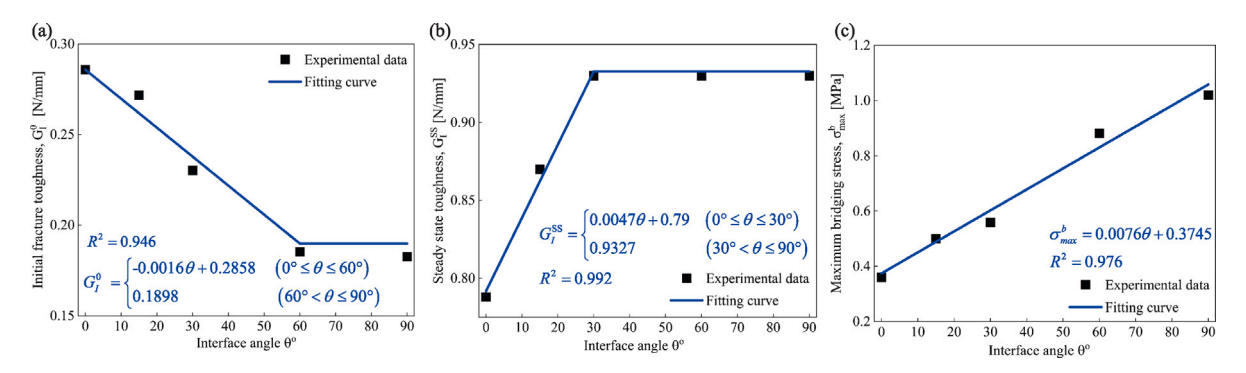


Fig. 9. The variations of (a) the initial fracture toughness G_I^0 , (b) the steady-state fracture toughness G_I^{ss} , and the maximum bridging stress σ_{max}^b with the interface angle θ .

As a result, the cohesive constitutive model in Fig. 7(a) can be obtained as follows:

$$\sigma(\delta) = \begin{cases} k_{\delta} & (\delta \leq \delta_{0}) \\ \left(\frac{\sigma_{max}^{b} - \sigma_{max}^{c}}{\delta_{1} - \delta_{0}}\right) \delta + \frac{\sigma_{max}^{c} \delta_{1} - \sigma_{max}^{b} \delta_{0}}{\delta_{1} - \delta_{0}} & (\delta_{0} < \delta \leq \delta_{1}) \\ \left(\frac{G_{a}}{\delta_{a}}\right) e^{-\frac{\delta - \delta_{1}}{\delta_{a}}} + \left(\frac{G_{b}}{\delta_{b}}\right) e^{-\frac{\delta - \delta_{1}}{\delta_{b}}} & (\delta_{1} \leq \delta \leq \delta_{f}) \\ 0 & (\delta > \delta_{f}) \end{cases}$$

$$(5)$$

Substitute the fitting parameters G_a , G_b , δ_a , and δ_b into the bridge stress model (Eq. (5)), where the opening displacement δ is in the range of $\delta_1 \leq \delta \leq \delta_f$ and the maximum fiber bridging stress σ^b_{max} at different interface angles can be calculated. The values are listed in the last column of Table 3. It is noteworthy that the fitting parameters are not explicitly related to the interface angle. Besides, these parameters may also be related to factors other than the interface angle. However, these parameters serve merely as intermediates for determining the relationship between the maximum traction force and the opening displacement δ , and are not essential for formulating a cohesion model. Alternative multi-parameter function forms may also exist, defining a relationship between maximum traction force and opening displacement δ . Thus, it is not necessary to explore the factors affecting these parameters in detail.

3.2. Simplified tri-linear cohesive constitutive model

To characterize how mode-I delamination cracks grow in the fiber-bridging zone at any given interface angle, it is essential to establish an explicit relationship between the fitting parameters and the interface angle within the traction cohesive constitutive model. We propose a simplified trilinear traction cohesive constitutive model, with parameters in the model related to the interface angle.

First, the variations of the initial fracture toughness G_I^0 and steady-state fracture toughness G_I^{ss} with interface angle are illustrated in Fig. 9(a) based on the data given in Table 2. It is noted that when the interface angle is less than 60°, the initial fracture toughness decreases linearly as the angle increases, whereas when the interface angle is between 60° and 90°, the initial fracture toughness remains constant as the angle increases. This trend aligns with the experimental findings of Pereira et al. [41] and Tohgo et al. [50]. The possible mechanism is that at a smaller fiber angle, stress concentration at the crack tip gradually increases. A change in the angle between the fiber direction and the load direction results in a more uneven stress distribution at the crack tip and increasing stress concentration. When the fiber angle is between 60° and 90°, the stress distribution approaches a stable mode. The initial fracture toughness of the material is expected to remain relatively stable despite variations in the interface fiber angle within this range. Fitting the experimental data provides a piecewise linear function of the initial fracture toughness G_I^0 with interface angle θ . Fig. 9(b) shows that when the interface angle is less than 30°, the steady-state fracture toughness increases linearly with the interface angle; when the interface angle is between 30° and 90°, the steady-state fracture toughness remains constant as the interface angle increases. The possible mechanisms are as follows: As the interface angle rises from 0° to 30°, the amount of fiber bridging increases, which enhances resistance to crack propagation and subsequently improves fracture toughness. As the interface angle increases, the degree of fiber bridging also increases; however, the length of the bridging area may decrease [40], thereby limiting the contribution of fiber bridging to fracture toughness. Consequently, when the interface angle exceeds 30°, the fracture toughness in the stable stage exhibits minimal variation with increasing interface angle. As a result, the piecewise linear function of the steady state fracture toughness G_I^{ss} with interface angle can be obtained by fitting. It must be pointed out that the fitting function does not consider experimental data for an interface angle of 45°. This data can be used to verify models. Thus, the function of the initial fracture toughness and the steady-state fracture toughness with the interface angle can be expressed as follows:

$$G_I^0(\theta) = \begin{cases} -0.0016\theta + 0.2858 & (0^{\circ} \le \theta \le 60^{\circ}) \\ 0.1898 & (60^{\circ} \le \theta \le 90^{\circ}) \end{cases}$$
 (6)

$$G_I^{ss}(\theta) = \begin{cases} 0.0047\theta + 0.79 & (0^{\circ} \le \theta \le 30^{\circ}) \\ 0.9327 & (30^{\circ} \le \theta \le 90^{\circ}) \end{cases}$$
 (7)

$$\sigma_{max}^b(\theta) = 0.0076\theta + 0.3745 \tag{8}$$

Next, the maximum bridging stress σ_{max}^b can be determined for different interface angles based on the cohesive constitutive model with the fitting parameters in Table 3 when the opening displacement δ is between δ_1 and δ_f , and the variation of the maximum bridging stress with the interface angle is plotted in Fig. 9(c). It is observed that when the interface angle ranges between 0° and 90° , the maximum bridging stress increases approximately linearly as the interface angle increases. This is because multi-directional laminated composites include many more bridging fibers during the delamination process than unidirectional laminated composites, as indicated in Fig. 5. As a result, the piecewise linear fitting function in Eq. (8) can be obtained accordingly. Then the crack opening displacement δ_1 can be determined using a linear relationship in the constitutive model when δ falls within the range of $\delta_0 < \delta < \delta_1$. The expression associated with the interface angle is given as follows:

$$\delta_1(\theta) = \frac{2kG_I^0(\theta) + \sigma_{max}^c \sigma_{max}^b(\theta)}{k(\sigma_{max}^b(\theta) + \sigma_{max}^c)} \tag{9}$$

Finally, the nonlinear relationship between the fiber bridging stress and crack opening displacement in the fiber-bridging zone in Fig. 7(a) can be simplified into a linear relationship in Fig. 7(b). The area covered by the triangle in red represents the fracture toughness caused by the fiber bridging and is determined by $G_I^b = G_I^{ss} - G_I^0$, the difference between the steady-state fracture toughness and the initial fracture toughness. The crack opening displacement δ_f at the end of the bridging zone is related to the interface angle θ , as shown below.

$$\delta_f(\theta) = \frac{2\left[G_I^{ss}(\theta) - G_I^0(\theta)\right]}{\sigma_{max}^b(\theta)} + \delta_1(\theta) \tag{10}$$

The nonlinear fiber bridging model has been converted to the linear bridging model in the fiber bridging zone. When comparing the two fiber bridging constitutive models in Fig. 7, we noticed that the two crack opening displacements of the end of the cohesive zone δ_f differ, given that the areas S_1 and S_2 in Fig. 7(a) are equal, the strain energy covered in the bridging zone, and the associated phenomenological constitutive behavior are equivalent. However, the crack opening displacement of the end of the cohesive zone in the bridging model is not an intrinsic property of the material. It is related to the mathematical form of the phenomenological bridging model and is obtained through experimental fitting. As a result, the tri-linear cohesive constitutive model in the delamination crack region can be given as follows:

$$\sigma(\theta) = \begin{cases} k_{\delta} & \delta \leq \delta_{0} \\ \frac{[\sigma_{max}^{b}(\theta) - \sigma_{max}^{c}]\delta}{\delta_{1}(\theta) - \delta_{0}} + \frac{\sigma_{max}^{b}(\theta)\delta_{0} + \sigma_{max}^{c}\delta_{1}(\theta)}{\delta_{1}(\theta) - \delta_{0}} & \delta_{0} < \delta \leq \delta_{1} \\ \frac{\sigma_{max}^{b}(\theta)[\delta_{f}(\theta) - \delta]}{\delta_{f}(\theta) - \delta_{1}(\theta)} & \delta > \delta_{1} \end{cases}$$

$$(11)$$

Fig. 7(b) presents the schematic diagram of the trilinear interface cohesive force constitutive model. The area of the blue region corresponds to the value of G_I^0 . The relationships between the G_I^0 and σ_{max}^b with the interface angle θ have been given by Eqs. (6) and (8) based on Fig. 9. Consequently, δ_1 can be derived using Eq. (9), given the known parameters k, σ_{max}^c , and σ_{max}^b . The initial interface stiffness k and the maximum stress σ_{max}^c at the onset of damage in the cohesive force constitutive model for different interface angles are determined through fitting to the DCB experimental results of the $0^{\circ}//0^{\circ}$ specimen. The fitting results yield k = 10000 and σ_{max}^c = 55 MPa. Thus, the opening displacement δ_0 at the damage initiation can be determined using the tri-linear cohesion constitutive model:

$$\delta_0 = \sigma_{max}^c / k \tag{12}$$

4. Results and discussion

4.1. Numerical model of DCB specimens

To validate the dependence of mode I fracture toughness on the interface angle as described by Eqs. (6) and (7), along with the interface tri-linear cohesion constitutive model, a three-dimensional finite element model of the double cantilever beam was constructed utilizing Abaqus' explicit solver. Fig. 10 illustrates the finite element model. The model's width is reduced to one-fifth of its original size to enhance efficiency [51,52]. As a result, the size of the double cantilever beam finite element model is 200 mm \times 5 mm \times 5 mm. The numerical analysis is conducted under displacement control using the linear loading method. The reference points RP-1 and RP-2 are established as 5 mm in the y direction from the midpoint of the upper edge of the upper beam side and the midpoint of the lower edge of the lower beam side. The displacements of reference points RP1 and RP2 are coupled to the upper and lower beam's y-z planes, respectively. Fig. 10 shows that a displacement of v=15 mm is applied in the y direction to the reference points RP-1 and RP-2, respectively. While the other end is fixed in the x, y, and z directions. The upper and lower cantilever beams utilize a total of 34,160 continuous shell elements (8-node SC8R). Cohesion elements (COH3D8), each with a thickness of 0.01 mm, are inserted between the upper and lower cantilever beams, yielding a total of 2,125 elements.

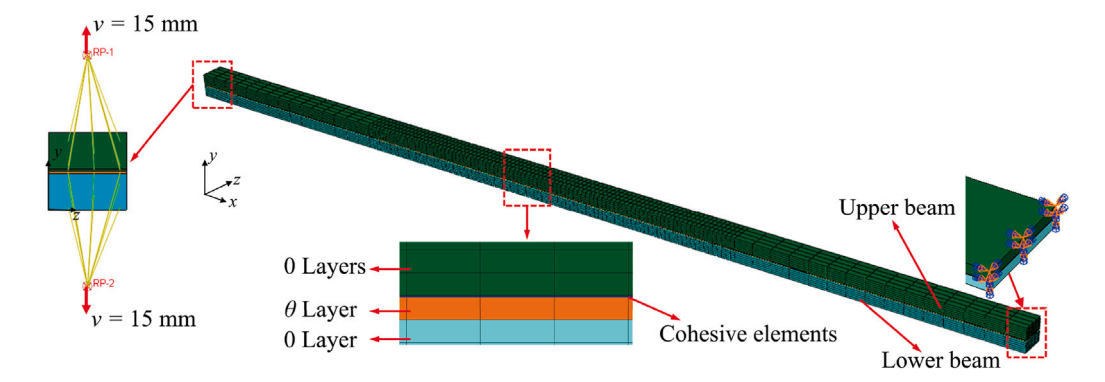


Fig. 10. The finite element model of the DCB laminate with cohesive elements.

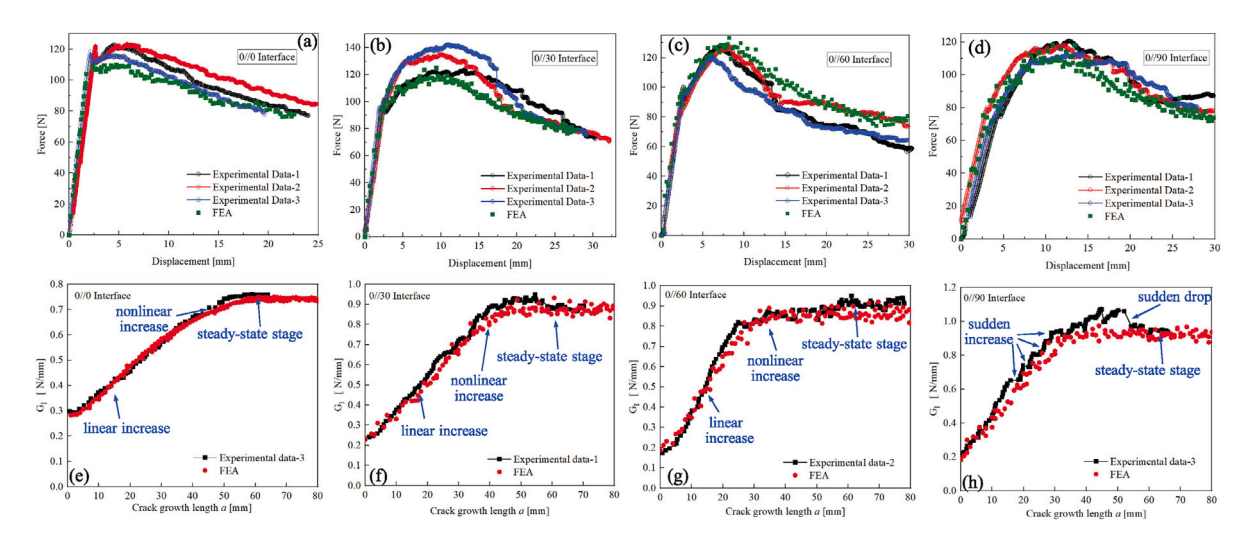


Fig. 11. Comparisons of the load–displacement curve and the fracture toughness variation with the delamination crack growth length obtained the DCB experiment and the numerical model. (a) and (e) $0^{\circ}//0^{\circ}$; (b) and (f) $0^{\circ}//30^{\circ}$; (c) and (g) $0^{\circ}//60^{\circ}$; (d) and (h) $0^{\circ}//90^{\circ}$.

The constitutive behavior of the interface with fiber bridge cohesion is implemented using the Abaqus user subroutine VUMAT. The opening displacement, δ , of the cohesive element is determined by the product of its strain and thickness. The cohesive element's stress is updated by assessing the opening displacement value δ and substituting it into Eq. (11). If the cohesive element's opening displacement δ is below δ_1 , the variable in the state storage 'StateNew' that tracks fiber bridging damage in the element is assigned a value of zero. When the cohesive element's opening displacement δ is larger or equal to δ_1 , the variable in the state storage StateNew that tracks fiber bridging damage in the element is assigned a value of 1. This indicates that fiber bridging damage occurs in the cohesive element at the current increment step. The delamination crack growth length, a, is defined as the distance from the beginning of delamination, where fiber bridging damage occurs, to the initial crack tip in the numerical model. In this study, an element is regarded as completely failed if its opening displacement δ exceeds δ_f . Consequently, the element is removed by adjusting the state storage variable StateNew in the subroutine. When the cohesive unit's opening displacement δ exceeds δ_f , the variable in the state storage StateNew that indicates element failure is set to 0, resulting in the deletion of the element by the program. At the present increment step, the cohesive element fails entirely, resulting in the forward propagation of the crack.

4.2. The delamination growth behavior at various interface angles

Fig. 11 presents a comparison of the load–displacement curve and the variation of fracture toughness with delamination crack growth length, as derived from the DCB experiment and the numerical model. The numerical model employs the cohesive traction–separation constitutive model at the interface angle, as indicated in Eq. (11). The initial and steady-state fracture toughness of the numerical model aligns with the experimental results. During the stage in which fracture toughness increases linearly with the length of delamination crack growth, the rate of fracture toughness growth obtained from numerical simulations closely aligns with the experimental findings. The comparison demonstrates a significant correlation between the experimental and numerical results, suggesting that the cohesive constitutive model derived from fitting the experimental data effectively captures delamination crack

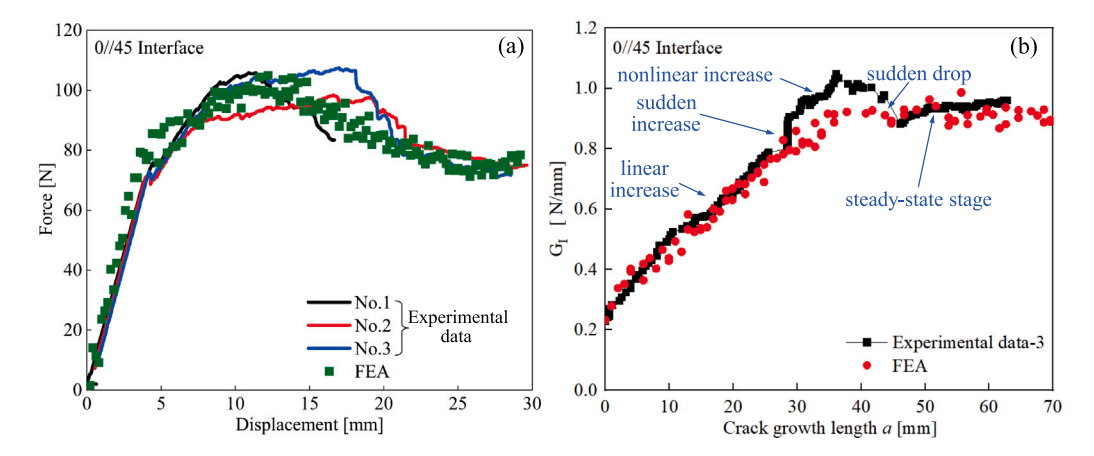


Fig. 12. Comparison of (a) the load–displacement curve and (b) the variation of the fracture toughness with the delamination crack length obtained by the DCB experiment and the numerical model at the $0^{\circ}//45^{\circ}$ interface.

growth. Additionally, Fig. 12 illustrates the load–displacement curve, the relationship between fracture toughness and delamination crack growth length derived from the DCB experiment, and the numerical model at the $0^{\circ}//45^{\circ}$ interface. The experimental results obtained for model verification were not utilized in determining the cohesive constitutive model. The results suggest that the cohesive constitutive model, derived from experimental data, is capable of predicting delamination crack growth behavior across various interface angles in the laminated specimen during the DCB experiment.

The experimental results presented in Figs. 11 and 12(b) indicate that the relationship between fracture toughness and delamination crack growth length for DCB specimens with varying interface angles exhibits several notable characteristics. Fracture toughness initially exhibits a linear increase with the growth length of delamination cracks, subsequently transitioning to a nonlinear increase until a maximum is attained. As the delamination crack length increases, the fracture toughness reaches a steady-state growth stage and remains constant, as illustrated in Figs. 11(e)–(g). Fracture toughness can exhibit discontinuities, characterized by sudden increases, a peak, followed by a rapid decrease, ultimately transitioning into a steady-state growth phase, as illustrated in Figs. 11(h) and 12(b). The numerical model effectively characterizes the transition of fracture toughness from linear to nonlinear as the delamination crack length increases until the steady-state stage is achieved. However, it fails to account for the discontinuous fluctuations and abrupt changes, as illustrated in Figs. 11(h) and 12(b). The comparison reveals a discrepancy between the numerical prediction of peak fracture toughness and the experimental findings. The numerical model fails to account for the discontinuous variation in fracture toughness, as the delamination crack propagation path may exhibit jumps during the growth of the delamination crack. The initiation of the jump in the propagation path requires more energy, which inhibits further delamination crack propagation and results in enhanced fracture toughness, representing the toughening mechanism. The post-test C-scan image of the specimen (Fig. 6) further corroborated this mechanism. Accurate capture of peak fracture toughness requires the numerical model to account for the jump toughening mechanism.

4.3. The effect of zigzag delamination on the fracture toughness of the DCB specimen

The C-scan results presented in Fig. 6 indicate that zigzag growth transpired during the delamination crack propagation of DCB specimens with differing interface angles. Figs. 11(h) and 12(b) show the relationship between fracture toughness and delamination crack length growth for specimens with $0^{\circ}//90^{\circ}$ and $0^{\circ}//45^{\circ}$ interface angles. There are several abrupt increases or a single increase followed by a sudden decrease after the peak fracture toughness is reached. Specimens with varying interface angles exhibited a toughening mechanism before reaching steady-state fracture toughness. The experimental results suggest a link between the toughening mechanism and the non-interfacial zigzag delamination crack growth behavior. A numerical model of the DCB specimen with a $0^{\circ}//90^{\circ}$ interface angle was developed to confirm the relationship between the toughening mechanism and zigzag delamination crack growth, utilizing the previously established tri-linear cohesive constitutive relationship and incorporating the zigzag delamination crack growth.

A numerical model is developed to characterize the zigzag delamination crack growth, incorporating an inclined crack with an inclination angle α ($\alpha=45^{\circ}$) for the DCB specimen, featuring a $0^{\circ}//90^{\circ}$ interface angle. The crack propagates through the θ ($\theta=90^{\circ}$) ply. Upon reaching the $\theta//0^{\circ}$ interface, the crack progresses a distance of $\bar{\delta}$ along the interface, with $\bar{\delta}$ defined as the ply thickness. The crack subsequently alters its growth direction and extends along $-\alpha$ ($-\alpha=-45^{\circ}$) within the θ ply. Upon reaching the $0^{\circ}//\theta$ interface, the growth extends a distance δ along this interface, subsequently leading to a zigzag crack formation. \bar{a} denotes the total length of zigzag delamination crack growth, indicating the actual zigzag crack length instead of the projected length in the longitudinal direction. The formation of the zigzag crack is illustrated in the zoomed-in inset of Fig. 13. All delaminations, including the inclined crack in the θ ply and the interfacial delamination crack in the model, are represented by the cohesive element exhibiting a tri-linear cohesive constitutive relationship as specified in Eq. (11).

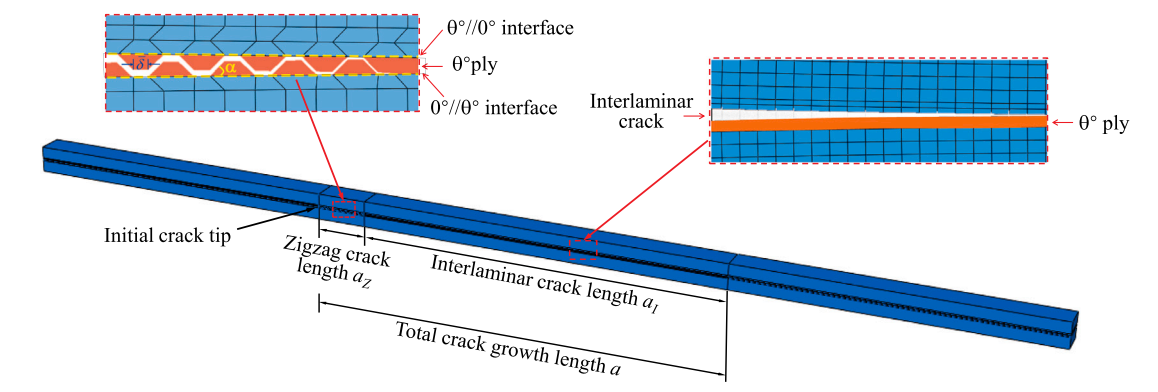


Fig. 13. FE model of the DCB specimen, which includes the zigzag crack and interlaminar delamination crack.

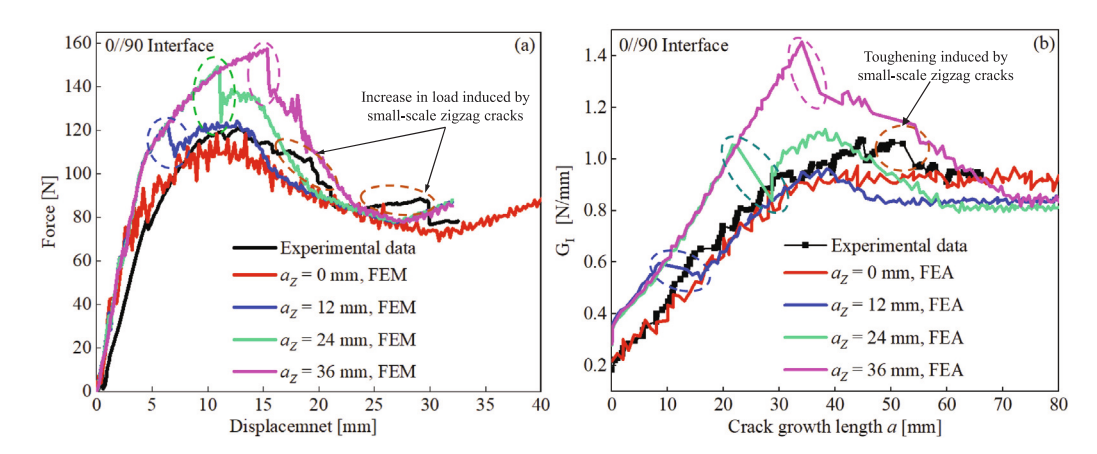


Fig. 14. (a) The load-displacement curve and (b) the variation of the fracture toughness with the crack length of the DCB specimen with 0°//90° interface angle obtained through numerical analysis with varying zigzag crack lengths.

Fig. 13 illustrates the finite element numerical model that accounts for zigzag crack propagation. The dimensions of the model align with those presented in Section 4.1. The COH3D8 cohesive element represents delamination cracks, including both inclined intralaminar cracks and interlaminar interface cracks. The SC8R continuous shell element is used for the upper and lower beams of the model. The model's boundary conditions align with Section 4.1.

Fig. 14(a) illustrates the load–displacement curve for the specimen with a $0^{\circ}//90^{\circ}$ interface angle, determined by numerical analysis incorporating different zigzag crack lengths, alongside a comparison with measured data. When there is no zigzag along the delamination crack propagation, that is, when $a_Z=0$, the load–displacement curve of the DCB specimen shows a linear rise, followed by a nonlinear rise. After the peak, we observe a monotonic, nonlinear decline until we reach a steady state. The presence of zigzag cracks significantly influences the load–displacement curve. Upon the transition from a zigzag crack to a non-zigzag interlaminar crack, the load–displacement curve demonstrates a swift decline. Consequently, it can be concluded that the transformation of non-zigzag interlaminar cracks into zigzag cracks during the DCB experiment may lead to a rapid increase in load, as indicated by non-monotonic small-amplitude fluctuations within the area delineated by the orange dotted line in Fig. 14(a). The alteration in the load–displacement curve may indicate the toughening mechanism associated with zigzag cracks. Nonetheless, the abrupt load variation in the measured load–displacement curve is less pronounced than in the numerical simulation. Detecting obvious load drops in the DCB experimental data is challenging due to the difficulty in forming a large-scale translaminar zigzag delamination crack that causes only a localized impact.

Fig. 14(b) shows how fracture toughness is related to the length of a delamination crack in a DCB specimen, taking into account different zigzag crack lengths. The numerical analysis indicates that the existence of a zigzag crack influences fracture toughness G_I , with the degree of this effect being correlated to the length of the zigzag crack. Initially, zigzag cracks form during the propagation of delamination cracks in the numerical model, leading to a sudden increase in fracture toughness. This indicates that zigzag cracks demonstrate higher initial fracture toughness than non-zigzag cracks. However, the amplitude of the increase is solely associated with the zigzag crack mode, independent of the actual length of the zigzag crack. The rate of increase in fracture toughness for the zigzag crack is slightly higher than that for the non-zigzag interlaminar crack; this rate remains largely unaffected by the length of the zigzag crack. However, the peak fracture toughness increases with the length of the zigzag crack in the numerical simulation. When the zigzag intralaminar crack transitions to a non-zigzag interlaminar crack, a substantial decrease in fracture toughness

occurs, followed by a nonlinear increase in fracture toughness as the interlaminar crack length increases. Ultimately, regardless of the existence of a zigzag crack within the total delamination crack length a, when the delamination crack growth reaches a steady-state stage, the fracture toughness stabilizes at a constant value, which correlates with the interface angle, as demonstrated in Eq. (7). In the DCB experiment, the presence of a zigzag crack in conjunction with interlaminar delamination crack propagation is expected to result in a non-monotonic increase in fracture toughness. The variation in fracture toughness for delamination crack growth length is depicted within the area indicated by the dotted line.

The numerical analysis shows that zigzag cracks may cause a sudden rise in fracture toughness as the length of the delamination crack changes. This refers to toughening. It leads to different fracture toughness peak values or non-monotonic changes in the fracture toughness evolution curves for different DCB specimens. Various modes of zigzag crack growth may yield different toughening effects, thereby requiring further numerical analysis. Steady-state fracture toughness is independent of the presence of partial zigzag cracks during delamination crack propagation and is solely determined by the interface angle. This study suggests that the multiple jumps in the evolution curve of fracture toughness related to delamination crack length may be linked to the formation of multiple zigzag cracks. This hypothesis requires validation through comprehensive C-scan results and further numerical analysis.

5. Conclusions

An experimental investigation was performed to analyze the mode-I fracture behavior of laminates with different interface angles, utilizing the digital image correlation (DIC) technique. A method is proposed that employs the grayscale correlation parameter of the subset in digital image correlation (DIC) to identify the location of the crack tip and the corresponding delamination crack length. The proposed method significantly reduces data processing and enhances measurement efficiency compared to the virtual extensometer method, while preserving the accuracy of crack propagation length measurements.

The experimental results demonstrate that both the initial fracture toughness and steady-state fracture toughness exhibit bilinear variation with the interface angle; however, the patterns of variation are distinct. The relationship between fracture toughness and delamination crack growth length indicates a toughening effect, characterized by a marked increase in fracture toughness before achieving a steady state at interface angles of 45° and 90°. We propose that small fluctuations in fracture toughness and the toughening mechanism may be associated with the transition of interlaminar cracks to irregular zigzag intralaminar cracks, as observed through C-scan analysis.

An explicit cohesive constitutive model is developed based on the bilinear relationship between initial fracture toughness and steady-state fracture toughness as a function of interface angle, utilizing the traction–separation law of the interface and experimental data. The cohesive constitutive model can be derived by fitting the DCB experimental data using a minimum number of three interface angles: 0°, 90°, and 30°. A prediction model for mode-I fracture behavior at various interface fiber angles is developed based on the explicit relationship and integrated into the finite element model of a double cantilever beam. The numerical model's characterization of delamination crack propagation behavior aligns well with the experimental results.

A finite element model incorporating a zigzag crack at the $0^{\circ}//90^{\circ}$ interface is developed. This study demonstrates a correlation between the enhancement of fracture toughness in laminate composites and the propagation of zigzag cracks. According to numerical analysis, zigzag cracks may increase the fracture toughness before they reach the steady-state fracture toughness. The peak fracture toughness correlates with the length of the zigzag cracks. The growth length of the irregular intralaminar crack in zigzag mode, when significantly shorter than that of the interlaminar interface crack, does not govern the propagation of delamination cracks. The zigzag crack's toughening effect does not impact the initial or steady-state fracture toughness of the interface crack. Consequently, its contribution to the cohesive constitutive model may be disregarded.

CRediT authorship contribution statement

Linlin Deng: Writing – original draft, Methodology, Investigation, Formal analysis. Liu Liu: Writing – review & editing, Validation, Supervision, Investigation, Funding acquisition. John-Alan Pascoe: Writing – review & editing, Supervision, Resources. René Alderliesten: Writing – review & editing, Supervision, Resources, Project administration, Conceptualization.

Declaration of competing interest

The authors declare that they have no known competing financial interests or personal relationships that could have appeared to influence the work reported in this paper.

Acknowledgments

This work is sponsored by the National Natural Science Foundation of China (No. 12472124, U2241240). Dr. L. Liu is supported under the 111 Project (B16003). Such support is gratefully acknowledged.

Data availability

Data will be made available on request.

References

- [1] May M. Measuring the rate-dependent mode Ifracture toughness of composites-A review. Compos Part A: Appl Sci Manuf 2016;81:1–12. http://dx.doi.org/10.1016/j.compositesa.2015.10.033.
- [2] Zhao M, Zhao Y, Wang A, Chang Z, Zhang J, Wang Z. Investigation of the mode-I delamination behavior of Double-Double laminate carbon fiber reinforced composite. Compos Sci Technol 2024;248:110463. http://dx.doi.org/10.1016/j.compscitech.2024.110463.
- [3] Rafiee R, Sotoudeh S. A hysteresis cohesive approach for predicting mixed-mode delamination onset of composite laminates under cyclic loading: Part I, model development. Compos Struct 2021;277:114667. http://dx.doi.org/10.1016/j.compstruct.2021.114667.
- [4] van de Kerk J, de Melo RF, Bastiani G, Donadon MV, Arbelo MA. A numerical and experimental study of fasteners as a delamination arrest mechanism in composite laminates under mode I loading. Thin-Walled Struct 2023;191:111047. http://dx.doi.org/10.1016/j.tws.2023.111047.
- [5] Khan R. Fiber bridging in composite laminates: A literature review. Compos Struct 2019;229:111418. http://dx.doi.org/10.1016/j.compstruct.2019.111418.
- [6] Salamat-Talab M, Shokrieh M, Mohaghegh M. On the R-curve and cohesive law of glass/epoxy end-notch flexure specimens with 0/θ interface fiber angles. Polym Test 2021;93:106992. http://dx.doi.org/10.1016/j.polymertesting.2020.106992.
- [7] Low KO, Johar M, Sung AN, Mohd Nasir MN, Rahimian Koloor SS, Petrû M, et al. Displacement rate effects on mixed-mode I/II delamination of laminated carbon/epoxy composites. Polym Test 2022;108:107512. http://dx.doi.org/10.1016/j.polymertesting.2022.107512.
- [8] Liu HH, Qi G, Renaud G, Li G, Li CL. Application of the effective crack length method to model delamination of unidirectional composite laminates under Mode II shear loadings. Compos Part C: Open Access 2023;12:100401. http://dx.doi.org/10.1016/j.jcomc.2023.100401.
- [9] ASTM D5528/D5528M-21, standard test method for mode I interlaminar fracture toughness of unidirectional fiber-reinforced polymer matrix composites. Tech. Rep., West Conshohocken, PA, USA: ASTM International; 2021, http://dx.doi.org/10.1520/D5528-D5528M-21.
- [10] Robinson P, Song D. A modified DCB specimen for mode I testing of multidirectional laminates. J Compos Mater 1992;26(11):1554–77. http://dx.doi.org/10.1177/002199839202601101.
- [11] Ubago Torres M, Jalalvand M. Additive binding layers to suppress free edge delamination in composite laminates under tension. Compos Part A: Appl Sci Manuf 2022;156:106902. http://dx.doi.org/10.1016/j.compositesa.2022.106902.
- [12] Shokrieh M, Salamat-talab M, Heidari-Rarani M. Dependency of bridging traction of DCB composite specimen on interface fiber angle. Theor Appl Fract Mech 2017;90:22–32. http://dx.doi.org/10.1016/j.tafmec.2017.02.009.
- [13] Kharratzadeh M, Shokrieh M, Salamat-talab M. Effect of interface fiber angle on the mode I delamination growth of plain woven glass fiber-reinforced composites. Theor Appl Fract Mech 2018;98:1–12. http://dx.doi.org/10.1016/j.tafmec.2018.09.006.
- [14] Bin Mohamed Rehan M, Rousseau J, Fontaine S, Gong X. Experimental study of the influence of ply orientation on DCBmode-I delamination behavior by using multidirectional fully isotropic carbon/epoxy laminates. Compos Struct 2017;161:1–7. http://dx.doi.org/10.1016/j.compstruct.2016.11.036.
- [15] Shokrieh M, Zeinedini A, Ghoreishi S. On the mixed mode I/II delamination R-curve of E-glass/epoxy laminated composites. Compos Struct 2017;171:19–31. http://dx.doi.org/10.1016/j.compstruct.2017.03.017.
- [16] Ardakani-Movaghati F, Taheri-Behrooz F, Esmaili A. Temperature effect on mode I fracture toughness of silica/glass/epoxy composites. Fatigue Fract Eng Mater Struct 2024;47(3):903–17. http://dx.doi.org/10.1111/ffe.14212.
- [17] Mohammad S, Fathollah T-B, Mazaher S-T. Critical strain energy release rate of woven carbon/epoxy composites subjected to thermal cyclic loading. Polym Compos 2022;43(9):6135–49. http://dx.doi.org/10.1002/pc.26919.
- [18] Hosseini MR, Taheri-Behrooz F, Salamat-talab M. Mode I interlaminar fracture toughness of woven glass/epoxy composites with mat layers at delamination interface. Polym Test 2019;78:105943. http://dx.doi.org/10.1016/j.polymertesting.2019.105943.
- [19] Hu P, Tao R, Li X, Lubineau G. Decomposing the coupling damage in mode I multidirectional delamination. Compos Sci Technol 2022;229:109684. http://dx.doi.org/10.1016/j.compscitech.2022.109684.
- [20] De Gracia J, Boyano A, Arrese A, Mujika F. Analysis of DCB test of angle-ply laminates including bending-twisting coupling. Compos Struct 2018;190:169–78. http://dx.doi.org/10.1016/j.compstruct.2018.02.021.
- [21] Reiner J, Torres JP, Veidt M. A novel top surface analysis method for mode I interface characterisation using digital image correlation. Eng Fract Mech 2017;173:107–17. http://dx.doi.org/10.1016/j.engfracmech.2016.12.022.
- [22] Khudiakova A, Grasser V, Blumenthal C, Wolfahrt M, Pinter G. Automated monitoring of the crack propagation in mode I testing of thermoplastic composites by means of digital image correlation. Polym Test 2020;82:106304. http://dx.doi.org/10.1016/j.polymertesting.2019.106304.
- [23] Zhu M, Gorbatikh L, Fonteyn S, Van Hemelrijck D, Pyl L, Carrella-Payan D, et al. Digital image correlation assisted characterization of Mode I fatigue delamination in composites. Compos Struct 2020;253:112746. http://dx.doi.org/10.1016/j.compstruct.2020.112746.
- [24] Rajan S, Sutton MA, Fuerte R, Kidane A. Traction-separation relationship for polymer-modified bitumen under Mode I loading: Double cantilever beam experiment with stereo digital image correlation. Eng Fract Mech 2018;187:404–21. http://dx.doi.org/10.1016/j.engfracmech.2017.12.031.
- [25] Gorman J, Thouless M. The use of digital-image correlation to investigate the cohesive zone in a double-cantilever beam, with comparisons to numerical and analytical models. J Mech Phys Solids 2019;123:315–31. http://dx.doi.org/10.1016/j.jmps.2018.08.013.
- [26] Blaysat B, Hoefnagels J, Lubineau G, Alfano M, Geers M. Interface debonding characterization by image correlation integrated with Double Cantilever Beam kinematics. Int J Solids Struct 2015;55:79–91. http://dx.doi.org/10.1016/j.ijsolstr.2014.06.012.
- [27] Huo X, Luo Q, Li Q, Sun G. Measurement of fracture parameters based upon digital image correlation and virtual crack closure techniques. Compos Part B: Eng 2021;224:109157. http://dx.doi.org/10.1016/j.compositesb.2021.109157.
- [28] Joki R, Grytten F, Hayman B, Sørensen B. Determination of a cohesive law for delamination modelling-accounting for variation in crack opening and stress state across the test specimen width. Compos Sci Technol 2016;128:49–57. http://dx.doi.org/10.1016/j.compscitech.2016.01.026.
- [29] Duan Q, Hu H, Cao D, Cai W, Li S. A new mechanism based cohesive zone model for Mode I delamination coupled with fiber bridging of composite laminates. Compos Struct 2024;332:117931. http://dx.doi.org/10.1016/j.compstruct.2024.117931.
- [30] Canal LP, Alfano M, Botsis J. A multi-scale based cohesive zone model for the analysis of thickness scaling effect in fiber bridging. Compos Sci Technol 2017;139:90–8. http://dx.doi.org/10.1016/j.compscitech.2016.11.027.
- [31] Karmakov S, Cepero-Mejías F, Curiel-Sosa J. Numerical analysis of the delamination in CFRP laminates: VCCT and XFEM assessment. Compos Part C: Open Access 2020;2:100014. http://dx.doi.org/10.1016/j.jcomc.2020.100014.
- [32] Heidari-Rarani M, Sayedain M. Finite element modeling strategies for 2D and 3D delamination propagation in composite DCB specimens using VCCT, CZM and XFEM approaches. Theor Appl Fract Mech 2019;103:102246. http://dx.doi.org/10.1016/j.tafmec.2019.102246.
- [33] Bouhala L, Makradi A, Belouettar S, Younes A, Natarajan S. An XFEM/CZM based inverse method for identification of composite failure parameters. Comput Struct 2015;153:91–7. http://dx.doi.org/10.1016/j.compstruc.2015.02.035.
- [34] Teimouri F, Heidari-Rarani M, Haji Aboutalebi F. An XFEM-VCCT coupled approach for modeling mode I fatigue delamination in composite laminates under high cycle loading. Eng Fract Mech 2021;249:107760. http://dx.doi.org/10.1016/j.engfracmech.2021.107760.
- [35] Airoldi A, Dávila CG. Identification of material parameters for modelling delamination in the presence of fibre bridging. Compos Struct 2012;94(11):3240–9. http://dx.doi.org/10.1016/j.compstruct.2012.05.014.
- [36] Yolum U, Bozkurt MO, Gok E, Coker D, Güler MA. Crack propagation in the double cantilever beam using Peridynamic theory. Compos Struct 2022;301:116050. http://dx.doi.org/10.1016/j.compstruct.2022.116050.

- [37] Sohrabi A, Pourhosseinshahi M, Mohammadi B. Prediction of mode I fracture behavior of delaminated 0//90 interface in cross-ply laminated composites from the SERR of classical unidirectional DCB specimen. Compos Struct 2023;317:117080. http://dx.doi.org/10.1016/j.compstruct.2023.117080.
- [38] Khan R. Delamination growth in composites under fatigue loading (Ph.D. thesis), Technische Universiteit Delft; 2013.
- [39] Daneshjoo Z, Shokrieh MM, Fakoor M, Alderliesten R, Zarouchas D. Physics of delamination onset in unidirectional composite laminates under mixed-mode I/II loading. Eng Fract Mech 2019;211:82–98. http://dx.doi.org/10.1016/j.engfracmech.2019.02.013.
- [40] Shokrieh M, Salamat-talab M, Heidari-Rarani M. Effect of interface fiber angle on the R-curve behavior of E-glass/epoxy DCB specimens. Theor Appl Fract Mech 2016;86:153-60. http://dx.doi.org/10.1016/j.tafmec.2016.06.006.
- [41] Pereira A, de Morais A. Mode I interlaminar fracture of carbon/epoxy multidirectional laminates. Compos Sci Technol 2004;64(13):2261–70. http://dx.doi.org/10.1016/j.compscitech.2004.03.001.
- [42] Andersons J, König M. Dependence of fracture toughness of composite laminates on interface ply orientations and delamination growth direction. Compos Sci Technol 2004;64(13):2139–52. http://dx.doi.org/10.1016/j.compscitech.2004.03.007.
- [43] Völkerink O, Koord J, Petersen E, Hühne C. Holistic determination of physical fracture toughness values and numerical parameters for delamination analysis considering multidirectional-interfaces. Compos Part C: Open Access 2022;8:100277. http://dx.doi.org/10.1016/j.jcomc.2022.100277.
- [44] Mekky W, Nicholson PS. The fracture toughness of Ni/Al2O3 laminates by digital image correlation I: experimental crack opening displacement and R-curves. Eng Fract Mech 2006;73(5):571–82.
- [45] Huo X, Luo Q, Li Q, Zheng G, Sun G. On characterization of cohesive zone model (CZM) based upon digital image correlation (DIC) method. Int J Mech Sci 2022;215:106921. http://dx.doi.org/10.1016/j.ijmecsci.2021.106921.
- [46] Zhu Y, Liechti KM, Ravi-Chandar K. Direct extraction of rate-dependent traction–separation laws for polyurea/steel interfaces. Int J Solids Struct 2009;46(1):31–51. http://dx.doi.org/10.1016/j.ijsolstr.2008.08.019.
- [47] Pan B, Xie H, Wang Z. Equivalence of digital image correlation criteria for pattern matching. Appl Opt 2010;49(28):5501–9. http://dx.doi.org/10.1364/AO.49.005501.
- [48] Ye J, Gong Y, Tao J, Cao T, Zhao L, Zhang J, et al. Efficiently determining the R-curve and bridging traction-separation relation of mode I delamination in a simple way. Compos Struct 2022;288:115388. http://dx.doi.org/10.1016/j.compstruct.2022.115388.
- [49] Gutkin R, Pinho S, Robinson P, Curtis P. On the transition from shear-driven fibre compressive failure to fibre kinking in notched CFRP laminates under longitudinal compression. Compos Sci Technol 2010;70(8):1223–31. http://dx.doi.org/10.1016/j.compscitech.2010.03.010.
- [50] Tohgo K, Hirako Y, Ishii H, Sano K. Mode I interlaminar fracture toughness and fracture mechanism of angle-ply Carbon/Nylon laminates. J Compos Mater 1996;30(6):650–61. http://dx.doi.org/10.1177/002199839603000601.
- [51] Yao L, Liu J, Lyu Z, Alderliesten R, Hao C, Ren C, et al. In-situ damage mechanism investigation and a prediction model for delamination with fibre bridging in composites. Eng Fract Mech 2023;281:109079. http://dx.doi.org/10.1016/j.engfracmech.2023.109079.
- [52] Cui H. Delamination and debonding failure of laminated composite t-joints (Ph.D. thesis), Technische Universiteit Delft; 2014.